

- [19] A. du Pasquier, P. C. Warren, D. Culver, A. S. Gozdz, G. G. Amatucci, J. M. Tarascon, *Solid State Ionics* **2000**, *135*, 249.  
 [20] P. P. Tsai, H. S. Gibson, P. Gibson, *J. Electrostatics* **2002**, *54*, 333.  
 [21] H. Yoshimoto, Y. M. Shin, H. Terai, J. P. Vacanti, *Biomaterials* **2003**, *24*, 2077.  
 [22] X. Wang, C. Drew, S.-H. Lee, K. J. Senecal, J. Kumar, L. A. Samuelson, *Nano Lett.* **2002**, *2*, 1273.  
 [23] K. K. Baumgarten, *J. Colloid Interface Sci.* **1971**, *36*, 71.  
 [24] M. Bognitzki, W. Czado, T. Frese, A. Schaper, M. Hellwig, M. Steinhart, A. Greiner, J. H. Wendorff, *Adv. Mater.* **2001**, *13*, 70.  
 [25] H. Fong, D. H. Reneker, *J. Polym. Sci., Part B: Polym. Phys.* **1999**, *37*, 3488.  
 [26] S. Kooimbhongshe, W. Liu, D. H. Reneker, *J. Polym. Sci., Part B: Polym. Phys.* **2001**, *39*, 2598.  
 [27] H. Fong, I. Chun, D. H. Reneker, *Polymer* **1999**, *40*, 4585.  
 [28] J.-Y. Lai, F.-C. Lin, C.-C. Wang, D.-M. Wang, *J. Membrane Sci.* **1996**, *118*, 49.  
 [29] M. Tazaki, R. Wada, M. Okabe, T. Homma, *J. Appl. Polym. Sci.* **1997**, *65*, 1517.  
 [30] H. Huang, S. L. Wunder, *J. Electrochem. Soc.* **2001**, *148*, A279.  
 [31] J. M. Tarascon, A. S. Gozdz, C. N. Schmutz, F. Shukoki, P. C. Warren, *Solid state Ionics* **1996**, *49*, 86.

## Synthesis of Aragonite Nanofilament Networks by Mesoscale Self-Assembly and Transformation in Reverse Microemulsions\*\*

By Mei Li, Benedicte Lebeau, and Stephen Mann\*

The integration of nanosized components into functional materials and devices requires new technologies that provide reproducible processing and assembly of nanostructures across extended length scales. Current chemical approaches usually involve the controlled organization of preformed nanoparticles into relatively simple close-packed superstructures by solvent evaporation,<sup>[1,2]</sup> molecular cross-linking,<sup>[3,4]</sup> or programmed recognition,<sup>[5–7]</sup> or through the use of patterned substrates.<sup>[8,9]</sup> In contrast, other studies have demonstrated the potential of direct methods, in which synthesis and self-assembly are coupled in situ to produce higher-order nanoparticle-based structures.<sup>[10]</sup> These reactions are undertaken in complex media, such as water-in-oil microemulsions or aqueous solutions containing anionic polyelectrolytes, and result in the spontaneous organization of incipient inorganic–organic nanoparticles by mesoscale assembly and transformation of stable or metastable building blocks.<sup>[11]</sup> In the latter case, remarkable complex higher-order architectures such as twisted bundles, cones, and helicoids, often with self-similar structure, are produced by aggregation and subsequent crystallization of surfactant–polymer-stabilized amorphous nanoparticles.<sup>[12–18]</sup>

A common feature of these organized materials is the spontaneous embedding of structures over multiple length scales, which arises as an emergent property of the system that is not directly related to the smallest building block but dependent on how these units evolve in time and space. For example, the slow transformation of surfactant-stabilized amorphous nanoparticles within colloidal aggregates can be strongly coupled with rearrangements of surface-adsorbed organic molecules such that the organization and morphology of the resulting nanocrystals are modulated according to the length scale of the growing structure. Although the mechanistic details require further elucidation (see Coelfen and Mann for details),<sup>[11]</sup> the degree of cooperativity associated with these mesoscale disorder–order transformations is strongly influenced by the surface charge and degree of hydration of the inorganic phase and surfactant headgroups. In microemulsion-based reactions, these can be controlled, respectively, by changes in the reactant molar ratio<sup>[10,12]</sup> and the number of water droplets per amorphous nanoparticle ( $n$ ),<sup>[18]</sup> for a constant  $[\text{H}_2\text{O}]/[\text{surfactant}]$  molar ratio ( $w$ ) equal to 10. In the latter case, changes in the value of  $n$  produced a range of organized hybrid surfactant–vaterite ( $\text{CaCO}_3$ ) nanostructures associated with the water-induced crystallization of alkylbenzenesulfonate-coated amorphous calcium carbonate (ACC) nanoparticles in water-in-isooctane sodium bis(2-ethylhexyl)sulfosuccinate (NaAOT) microemulsions. Here, we extend these studies to a detailed investigation of the reaction system at an increased  $w$  value of around 20. Surprisingly, no vaterite nanostructures are formed under these conditions. Instead, remarkable doughnut-shaped micrometer-sized particles with mesoporous sponge-like internal structures consisting of interlinked aragonite nanofilaments are produced by the surfactant-mediated transformation and crystallization of the ACC precursor nanoparticles. Although nanofilament networks and mesoporous phases are rare for calcium carbonates, such materials could have important uses as catalyst supports, fillers, and pigments, as well as in the design of novel biomimetic scaffolds for targeted drug release and tissue engineering.<sup>[19]</sup>

Addition of dry samples of surfactant-stabilized ACC nanoparticles to NaAOT microemulsions prepared in isooctane at  $w=20$  and  $n=680$  produced transparent solutions that became slightly turbid within 30 min and cloudy after 2 h, followed by the gradual appearance of a white precipitate at the bottom of the test-tube. Powder X-ray diffraction analysis ( $d$ -spacings ( $hkl$  indices): 0.336 (111), 0.287 (002), 0.269 (012), 0.248 (200), 0.234 (130), 0.197 (221), 0.187 (202) nm) and Fourier transform infrared (FTIR) spectroscopy (vibrational bands; 700, 712, 864, 1082, and 1476  $\text{cm}^{-1}$ ) indicated that the precipitate collected after 5 h was aragonite. In addition, FTIR spectra of the as-prepared samples showed bands corresponding to ester C=O (1735  $\text{cm}^{-1}$ ), ester C=O, and S=O (1219  $\text{cm}^{-1}$ ), C=C aromatic (1595 and 1467  $\text{cm}^{-1}$ ), C–H methyl (2960, 2874  $\text{cm}^{-1}$ ), C–H methylene (2931, 2861  $\text{cm}^{-1}$ ), and O=S=O (1169  $\text{cm}^{-1}$ ) vibrations, indicating that significant amounts of alkylbenzenesulfonate and NaAOT were associated with the precipitate. This was confirmed by energy dis-

[\*] Prof. S. Mann, Dr. M. Li  
 School of Chemistry, University of Bristol  
 Bristol BS8 1TS (UK)  
 E-mail: s.mann@bris.ac.uk  
 Dr. B. Lebeau  
 Laboratoire de Matériaux Minéraux  
 CNRS UMR 7016, ENSCMu, UHA  
 3 rue Alfred Werner, F-68093 Mulhouse Cedex (France)

[\*\*] We thank Dr. Julian Eastoe for the gift of surfactant-stabilized amorphous calcium carbonate particles, Dr. Alex Kulak for technical expertise, and EPSRC for financial support to ML.

persive X-ray (EDX) analysis, which showed peaks for calcium (3.7, 4.0 keV), sulfur (2.3 keV), and sodium (1.0 keV), as well as thermogravimetric analysis (TGA), which indicated a surfactant content of ca. 20 wt.-% in the aragonite deposit.

Scanning electron microscopy (SEM) images of as-synthesized samples collected after 5 h showed that the precipitate consisted of a highly monodisperse distribution of doughnut-shaped particles with a mean size of 2.8  $\mu\text{m}$  ( $\sigma=0.3 \mu\text{m}$ ,  $n=50$ ). Washing the samples in ethanol–water removed most of the surfactant molecules (FTIR spectroscopy results not shown) to reveal particles with significantly increased surface definition and porosity (Fig. 1a). High-resolution SEM images indicated that the washed particles comprised densely packed layers of perforated plate-like crystals arranged at progressively increasing angles to the radial axis (Fig. 1b).

Transmission electron microscopy (TEM) and electron diffraction studies showed that individual layers of the surfactant-free doughnut-shaped particles consisted of a continuous sponge-like structure of convoluted branch-like aragonite nanofilaments (Fig. 2a), which were often less than 20 nm in width and separated by pores 10 to 50 nm in size. Sonicating the samples for 15 min in water resulted in extensive fragmentation of the mesoporous framework to produce individual aragonite nanoparticles that were 12 nm in mean width and

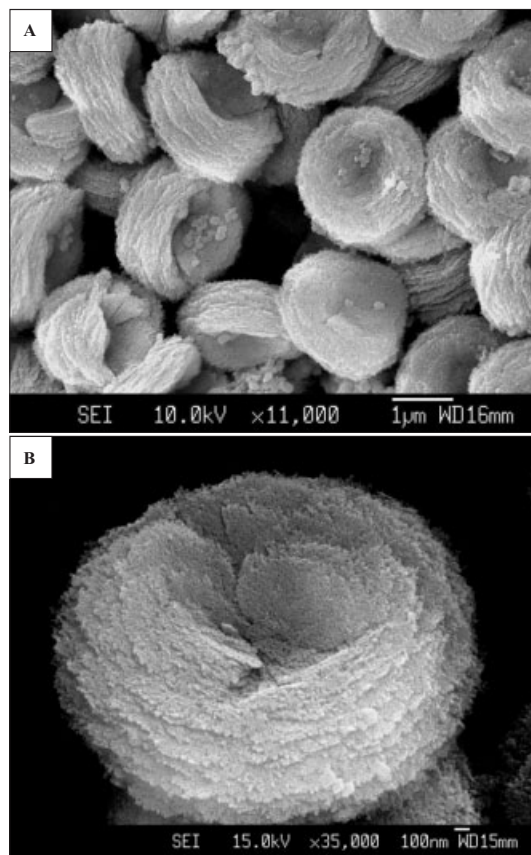


Fig. 1. SEM images: a) doughnut-like aragonite particles after surfactant removal; scale bar = 1  $\mu\text{m}$ . b) High-magnification image of a single aragonite particle showing multilayered ordering and sponge-like texture. Scale bar = 100 nm.

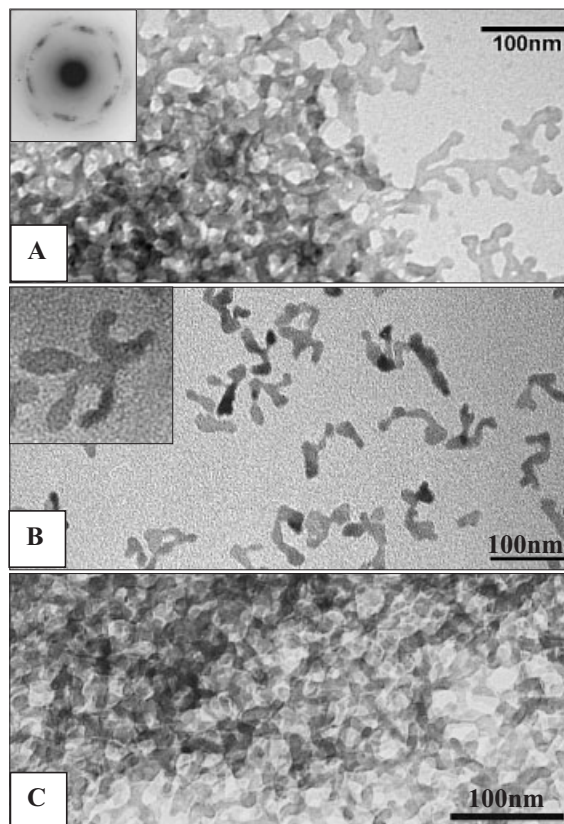


Fig. 2. TEM images: a) thin edge of as-synthesized doughnut-like aragonite particle showing porous network of branch-like crystalline nanofilaments. Inset: corresponding electron diffraction pattern showing aragonite reflections with  $d$ -spacings of 0.422 (110), 0.336 (111), 0.247 (200), 0.234 (130), 0.211 (220), 0.197 (221), 0.189 (041), and 0.124 (400) nm; b) aragonite nanoparticles with complex morphology produced by sonication-induced fragmentation; inset shows individual fragment; c) mesoporous aragonite sponge produced by aggregation and in situ fragmentation of doughnut-like structures. Scale bars = 100 nm.

generally less than 50 nm in length. The crystalline particles displayed a range of remarkable nanoscale sculptures such as squiggles, stirrups, and complex multipedes (Fig. 2b). Samples collected after 7 h showed a progressive reduction in the number of doughnut-shaped structures observed by electron microscopy due to interpenetration and associated disintegration of the multi-layered particles within larger aggregates. After two days, intermeshed aragonitic networks often several micrometers in size and with an intact sponge-like mesoporous texture were observed (Fig. 2c).

Nitrogen adsorption–desorption measurements on the as-synthesized and surfactant-free doughnut-shaped particles showed type IIb isotherms characteristic of macroporous/mesoporous materials with a large pore size distribution and Brunauer–Emmett–Teller (BET) surface areas of ca. 110 and 85  $\text{m}^2 \text{g}^{-1}$ , respectively (Fig. 3a). The Barrett–Joyner–Halenda (BJH) adsorption/desorption average pore diameters were 8.7/8.6 and 14.6/12.5 nm, respectively. Calcination of the as-synthesized samples at 400  $^\circ\text{C}$  for 1 h gave a macroporous aragonite with BET type III isotherm and surface area of ca. 45  $\text{m}^2 \text{g}^{-1}$  and BJH adsorption and desorption average pore diameters of 40.6 and 41.5 nm, respectively, with a narrow pore

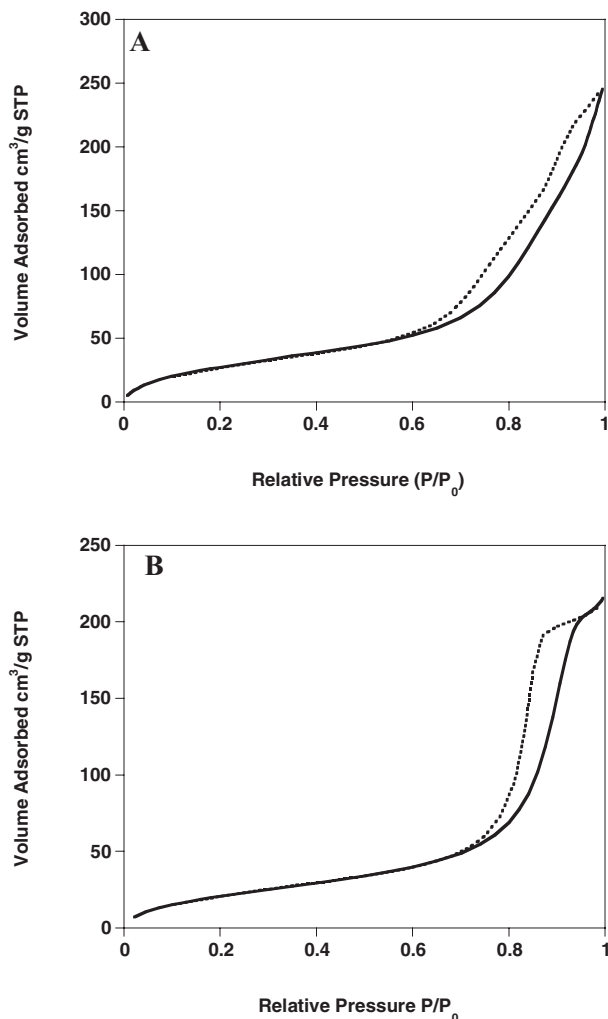


Fig. 3. Nitrogen adsorption (solid line) and desorption (dashed line) isotherms; a) as-synthesized sample; b) sponge-like aragonite network produced by aging for 2 days in the reaction solution.

size distribution. Significantly, the sponge-like fragments obtained after disintegration of the doughnut-shaped showed a well-defined type IV isotherm corresponding to a mesoporous material with a BET surface area of  $85 \text{ m}^2 \text{ g}^{-1}$  (Fig. 3b). BJH adsorption and desorption average pore diameters were 12.3 and 10.6 nm, respectively, with a relatively narrow sharp pore size distribution, consistent with the TEM results.

Time-dependent TEM studies indicated that the early stages of formation of the multi-layered aragonite particles in the microemulsions involved self-aggregation of the 5 nm sized surfactant-stabilized ACC nanoparticles (Fig. 4a). This was followed by growth of the colloidal aggregates and in-situ crystallization of the coalesced nanoparticles to produce aragonite disks. After 1 h, the disks were about 600 nm in diameter and consisted of several stacked layers, each with a particulate rather than porous texture (Fig. 4b). Subsequent growth, principally around the rim of the primary disks by further aggregation of the ACC precursor nanoparticles gave rise to micrometer-sized doughnut-shaped mesoporous crys-

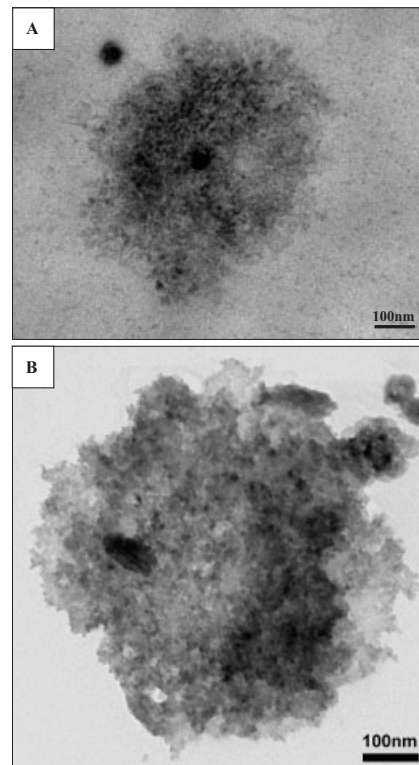


Fig. 4. TEM images of early growth stages of doughnut-like aragonite particles. a) After 40 min showing aggregated cluster of ACC nanoparticles. b) After 1 h, showing developing aragonite disk consisting of layers of aggregated nanocrystals. Scale bars = 100 nm.

tals within 2 h of mixing the reactants. Other studies indicated that the assembly of these crystals occurred within a relatively narrow range of conditions; viz.  $w = 18\text{--}22$  for  $[\text{H}_2\text{O}]/[\text{NaAOT}]/[\text{CaCO}_3]$  molar ratios between 620:34:1 and 760:34:1. In contrast, a mixture of fibrous and doughnut-like particles were observed at  $w = 15$  ( $[\text{H}_2\text{O}]/[\text{NaAOT}]/[\text{CaCO}_3] = 517:34:1$ ), whereas loose aggregates of irregular particles were observed at  $w = 25$  and  $[\text{H}_2\text{O}]/[\text{NaAOT}]/[\text{CaCO}_3] = 862:34:1$ .

The above results, as well as those of previous studies,<sup>[18]</sup> suggest that the nanostructures originate from a dissolution–reprecipitation process that is locally confined within nanoparticle aggregates and directed by surface interactions involving adsorbed surfactant molecules. The transformation processes are also dependent on the relative solubilities and surface stabilities of the ACC precursor and crystalline polymorphs of calcium carbonate. In this regard, the amount of water trapped within individual droplets, as well as the number of water droplets, had a marked effect on the polymorph structure, nanoscale morphology and organization, and higher-order architecture. Previous investigations<sup>[18]</sup> at  $w = 10$  indicated that strong coupling between the growing vaterite nanocrystals and sulfonate surfactant molecules occurred in the presence of low amounts of water ( $n = 34$ ) to give spheroidal aggregates of densely packed 5 nm sized nanoparticles, whereas weak interactions ( $n = 3400$ ) produced discrete vaterite nanoparticles, 130 nm in size. In contrast, intermediate lev-

els of coupling produced anisotropic nanostructures such as spindle-shaped aggregates of 18 nm sized vaterite nanoparticles ( $n=170$ ) or high aspect ratio twisted bundles of co-aligned 10 nm wide vaterite nanofilaments ( $n=340$ ), both of which were assembled by surfactant interdigitation between adjacent nanocrystals.

Increasing the diameter of the water droplets from ca. 4.5 nm ( $w=10$ ) to 6.5 nm ( $w=20$ ) results in formation of the less soluble polymorph, aragonite, possibly because there is now sufficient water in each droplet to dissolve both the ACC precursor and incipient vaterite nuclei. However, the subsequent growth of the aragonite crystals within the hybrid aggregates is strongly influenced by the presence of the closely associated surfactant molecules as demonstrated by the morphological complexity of the aragonite nanofilaments and their organization into an extended mesoporous framework. The branched and highly convoluted network of nanofilaments suggests that growth is confined to a percolated network of nanoscale water channels present within gel-like aggregates of a disordered surfactant mesophase. Each aggregate transforms initially into a compact surfactant–aragonite disk, followed by outgrowth from the rim of thin porous sheets of interconnected aragonite nanofilaments to produce the doughnut-like morphology of the micrometer-sized particles. Moreover, the high monodispersity in particle size suggests that the initial transformation of the ACC–surfactant aggregates into the aragonite disks occurs homogeneously throughout the reaction system within a relatively narrow time period. It is noteworthy that aragonite is nucleated under these conditions rather than the more thermodynamically stable polymorph, calcite. In the absence of  $Mg^{2+}$  ions, deposition of aragonite is relatively uncommon at room temperature, and further work is required to elucidate the factors that result in the selectivity of this polymorph in microemulsion-based reaction media.

Finally, a number of recent studies have demonstrated that the synthesis of CdTe or ZnO nanoparticles with polytypic structure can result in tetrapod-branched nanocrystals.<sup>[20,21]</sup> The synthesis of nanoparticles with complex non-symmetry-related shapes, such as the squiggles, stirrups, and convoluted multipedes prepared by fragmentation of the sponge-like aragonite networks described above, has not previously been demonstrated. Such nanosculptures represent a range of novel inorganic small-scale forms that could have important applications as speciality additives in materials such as paper, textiles, biomedical implants, inorganic–organic polymer nanocomposites, and powder-based products in general.

## Experimental

Analytical grade sodium bis(2-ethylhexyl)sulphosuccinate (NaAOT) and iso-octane (2,2,4-trimethylpentane) were purchased from BDH and Aldrich, respectively, and used without further purification. Alkybenzenesulfonate-stabilized (average chain length,  $n-C_{24}$ ) ACC nanoparticles were a gift from Dr. J. Eastoe (University of Bristol). The sample, which was dried by rotary evaporation, was similar to the “V-series” characterized previously [22]. CHN elemental analysis (total C = 41.75 %, N = 0 %, H = 5.89 %, inorganic C = 3.46 %) and thermogravimetric analysis (Simultaneous Thermal Analysis STA409EP) indicated that the amorphous nanoparticles contained 29 % (wt./wt.)  $CaCO_3$ . FTIR spectroscopy showed bands at 863  $cm^{-1}$  and 1079  $cm^{-1}$  corresponding to the  $CO_3^{2-}$  anion in amorphous  $CaCO_3$ , as well as at 1495  $cm^{-1}$  (C=C aromatic), 2958, 2927, and 2856  $cm^{-1}$  (C–H stretches), and 1183  $cm^{-1}$  (O=S=O symmetric stretch). Suspensions of surfactant-capped ACC nanoparticles in pure toluene were transparent stable solutions, which when air-dried onto TEM grids showed non-aggregated electron dense amorphous cores, ca. 5 nm in diameter.

Water-in-oil NaAOT microemulsions were prepared by adding small amounts of distilled water (pH=7.3) to NaAOT iso-octane solutions (0.1 M) to give  $w$  values ( $w=[H_2O]/[NaAOT]$ ) between 15 and 25. Typically, 3.6 mL of water was added to 100 mL of the 0.1 M NaAOT iso-octane solution to give a  $w$  value of 20. Dried samples of the alkybenzenesulfonate-capped ACC nanoparticles (100 mg) were added to the NaAOT microemulsion (100 mL) to give a  $CaCO_3$  final concentration of 3 mM (measured against total microemulsion volume) and  $[H_2O]/[NaAOT]/[CaCO_3]=680:34:1$ . The dispersions were shaken vigorously and then left to stand at room temperature without stirring. Samples for analysis were collected by centrifugation after periods between 30 min and two weeks. Excess surfactants were removed by washing with ethanol followed by centrifugation and washing three times with a 1:1 mixture of aqueous NaCl (0.1 M) and ethanol.

Samples for TEM, electron diffraction, and EDX analysis were deposited onto carbon-coated, 3 mm diameter, copper electron microscope grids. After drying in air, the grids were washed with pure iso-octane. TEM analysis was performed in bright field mode using a JEOL 1200 EX and JEM 2010 electron microscopes operating at 120 and 200 keV, respectively, and linked with an Oxford Instruments X-ray analysis system. Samples for SEM were mounted onto circular aluminum stubs or carbon adhesive pads attached to aluminum stubs. Samples were air-dried and platinum-coated with an Edwards S150B sputter-coater. SEM analyses were carried out using JEOL JSM 5600 LV and JEOL JSM 6300F FEGSEM scanning electron microscopes operating at accelerating voltages between 1–30 and 0.5–30 keV, respectively. Samples were studied by powder XRD (D8 advance X-ray diffractometer), TGA (simultaneous thermal analysis STA409EP), and FTIR spectroscopy (Perkin Elmer Spectrum One FTIR Spectrometer) using KBr disks. Nitrogen adsorption–desorption experiments were performed on a MICROMERITICS instrument ASAP 2010 type to determine BET surface area and porosity. Samples were degassed under vacuum at 90 °C for 15 h prior to analysis. Errors on the BJH adsorption and desorption average pore diameter data were 10 %.

Received: June 24, 2003

Final version: August 12, 2003

Published online: October 16, 2003

- [1] C. B. Murray, C. R. Kagan, M. G. Bawendi, *Science* **1995**, 270, 1335.
- [2] Z. L. Wang, *Adv. Mater.* **1998**, 10, 13.
- [3] R. P. Andres, J. D. Bielefeld, J. I. Henderson, D. B. Janes, V. R. Kolagunta, C. P. Kubiak, W. Mahoney, R. G. Osifchin, *Science* **1996**, 273, 1690.
- [4] M. Brust, D. Bethell, D. J. Schiffrin, C. J. Kiely, *Adv. Mater.* **1995**, 7, 795.
- [5] C. A. Mirkin, R. L. Letsinger, R. C. Mucic, J. J. Storhoff, *Nature* **1996**, 382, 607.
- [6] S. Mann, W. Shenton, M. Li, S. Connolly, D. Fitzmaurice, *Adv. Mater.* **2000**, 12, 147.
- [7] E. Dujardin, L.-B. Hsin, C. R. C. Wang, S. Mann, *Chem. Commun.* **2001**, 1264.
- [8] P. Yang, A. H. Rizvi, B. Messer, B. F. Chmelka, G. M. Whitesides, G. D. Stucky, *Adv. Mater.* **2001**, 13, 427.
- [9] W. Shenton, D. Pum, U. B. Sleytr, S. Mann, *Nature* **1998**, 389, 585.
- [10] M. Li, H. Schnablegger, S. Mann, *Nature* **1999**, 402, 393.
- [11] H. Coelfen, S. Mann, *Angew. Chem.* **2003**, 42, 2350.
- [12] M. Li, S. Mann, *Langmuir* **2000**, 16, 7088.
- [13] M. Antonietti, M. Breulmann, C. G. Göltner, H. Cölfen, K. K. W. Wong, D. Walsh, S. Mann, *Chem. Eur. J.* **1998**, 4, 2491.
- [14] L. M. Qi, H. Cölfen, M. Antonietti, M. Li, J. D. Hopwood, A. J. Ashley, S. Mann, *Chem. Eur. J.* **2001**, 7, 3526.
- [15] D. B. Zhang, L. M. Qi, J. M. Ma, H. M. Cheng, *Chem. Mater.* **2001**, 13, 2753.
- [16] A. Peytcheva, H. Cölfen, H. Schnablegger, M. Antonietti, *Colloid Polym. Sci.* **2002**, 280, 218.
- [17] S. H. Yu, H. Cölfen, M. Antonietti, *Chem. Eur. J.* **2002**, 8, 2937.
- [18] M. Li, S. Mann, *Adv. Funct. Mater.* **2002**, 12, 773.
- [19] D. Green, D. Walsh, S. Mann, R. O. C. Oreffo, *Bone* **2002**, 30, 81.
- [20] L. Manna, D. J. Milliron, A. Meisel, E. C. Scher, P. Alivisatos, *Nat. Mater.* **2003**, 2, 382.
- [21] Y. Dai, Y. Zhang, Q. K. Li, C. Nan, *Chem. Phys. Lett.* **2002**, 358, 83.
- [22] I. Markovic, R. H. Ottewill, *Colloid Polym. Sci.* **1986**, 264, 454.